ACS APPLIED MATERIALS & INTERFACES

www.acsami.org

Research Article

# Direct Observation of Li Migration into $V_5S_8$: Order to Antisite Disorder Intercalation Followed by the Topotactic-Based Conversion Reaction

Shulin Chen, Chen Yang, Ruiwen Shao, Jingjing Niu, Mei Wu, Jian Cao, Xiumei Ma, Jicai Feng, Xiaosong Wu, Jing Lu,* Liping Wang,* Junlei Qi,* and Peng Gao*

Cite This: ACS Appl. Mater. Interfaces 2020, 12, 36320–36328

Read Online

ACCESS | Metrics & More | Article Recommendations | Supporting Information



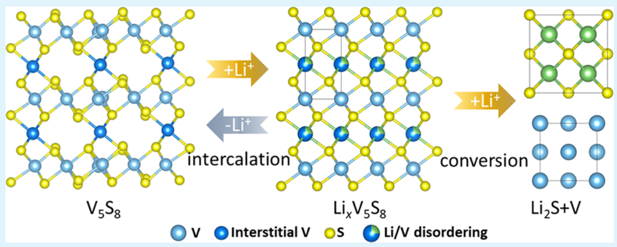


**ABSTRACT:** Two-dimensional transition-metal dichalcogenides hold great potential in rechargeable lithium-ion batteries. Their electrochemical properties are closely related to the structural evolutions during lithium-ion migration. Understanding these migration/reaction mechanisms is important to help improve battery performance. Herein, we report the real-time and atomic-scale observation of phase transitions during the lithiation and delithiation for $V_5S_8$ via in situ electron diffraction and high-resolution transmission electron microscopy techniques. We find that the phase transformation proceeds via a sequence of order to antisite disorder intercalation and topotactic-based conversion reaction. During the intercalation reaction, the lithium ion destroys the orderings of the interstitial V with the formation of Li/V antisite. Such a reaction is found to be reversible, i.e., the extraction of lithium from $Li_xV_5S_8$ leads to the recovery of V orderings. The conversion reaction involves heterogeneous nucleation of $Li_2S$ with 3−20 nm nanodomains, which maintain the crystallographic integrity with $Li_xV_5S_8$. These findings elucidate the complex interactions between the lithium ion and host $V_5S_8$ during ionic migration in solids, which should be helpful in understanding the relationship between phase transformation kinetics and battery performance.

**KEYWORDS:** *in situ TEM, transition-metal chalcogenide, lithium-ion migration, Li/V antisite, topotactic growth of $Li_2S$*

## 1. INTRODUCTION

Rechargeable lithium-ion batteries (LIBs) have been used as an efficient energy storage device in portable electronics and electric vehicles.[1−3] The ever-growing demand for unique applications such as ultrafast discharging−charging, super large capacities, and high output power necessitates searching and developing new electrode materials. Transition-metal dichalcogenides (TMDs) have been extensively explored as promising anodes[4,5] in LIBs due to their two-dimensional (2D) layered stacking structure through weak van der Waals interactions, which facilitates the fast alkaline ions transport.[6] These TMDs have demonstrated good Li-storage capacities via complex reactions including intercalation, conversion, and alloying reaction.[7−10] It is reported that the inserted lithium ions trigger different phase transformations via different pathways, such as 2H to 1T transition in $MoS_2$,[11−13] disordering transition[14] and intermediate superstructure[15] in $SnS_2$, two-phase transition in $TiS_2$,[16−18] metal extrusion in $CuS_2$,[19] and anisotropic lithiation in $ReS_2$.[20] These diverse lithiation pathways generate different intermediate or final products, which in turn influence the reaction reversibility, energy efficiency, and battery cyclability.[21,22] Therefore, it is important to investigate the reaction pathway and phase transformation to improve battery performance.

Metallic $VS_2$ has a large interlayer spacing of 5.67 Å,[23] which processes a high energy density and good reversibility as an anode material for LIBs.[24,25] $V_5S_8$ is another member of vanadium sulfides family that consists of ordered V within the interlayers, occupying one-quarter of available S−S octahedral sites and linking the two adjacent $VS_2$ monolayers. Such a three-dimensional structure can overcome the drawback of a 2D structure with anisotropic diffusion, which requires more engineering to align the crystal planes with the diffusional direction to achieve large insertion efficiency.[26] Moreover, the metallic nature of $V_5S_8$ is beneficial to the transport of electrons. These aspects enable $V_5S_8$ to be used in not only Li but Na and K ion batteries with good electrochemical performance.[27−29] For example, $V_5S_8$/C delivers high discharge and charge capacity of 1245 and 1112 mAh $g^{-1}$ at 0.1 A $g^{-1}$ and the capacity is maintained at 846 mAh $g^{-1}$ after 700 cycles at 1 A $g^{-1}$ for LIBs. With the current density increased

Received: May 11, 2020
Accepted: July 15, 2020
Published: July 15, 2020

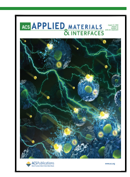




https://dx.doi.org/10.1021/acsami.0c08428
ACS Appl. Mater. Interfaces 2020, 12, 36320−36328

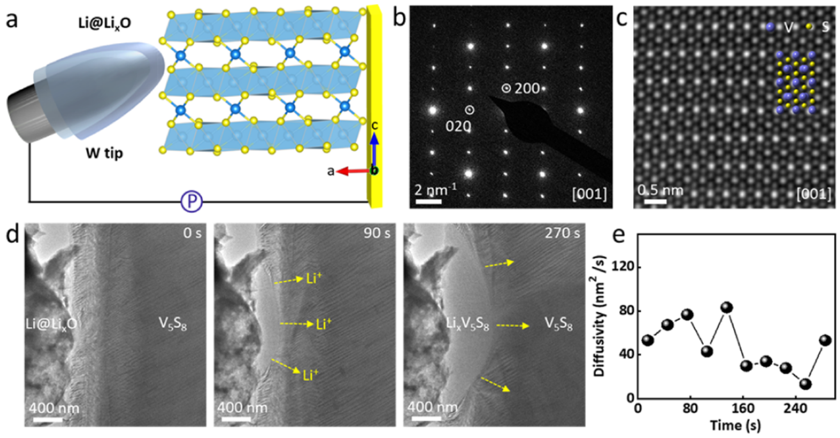

**Figure 1.** In situ lithiation of a $V_5S_8$ nanosheet. (a) In situ TEM setup, including a metallic lithium probe, a thin passivation layer of $Li_xO$, and a $V_5S_8$ nanosheet. (b) SAED pattern along the [001] direction and (c) corresponding atomically resolved HAADF-STEM image. The purple balls indicate V and yellow balls represent S. (d) Time-series TEM images during the lithiation of a $V_5S_8$ nanosheet. A clear boundary between $V_5S_8$ and $Li_xV_5S_8$ can be observed. The yellow arrows roughly indicate the diffusion directions of lithium ions. (e) Estimated diffusivity of lithium ions is plotted as a function of time.

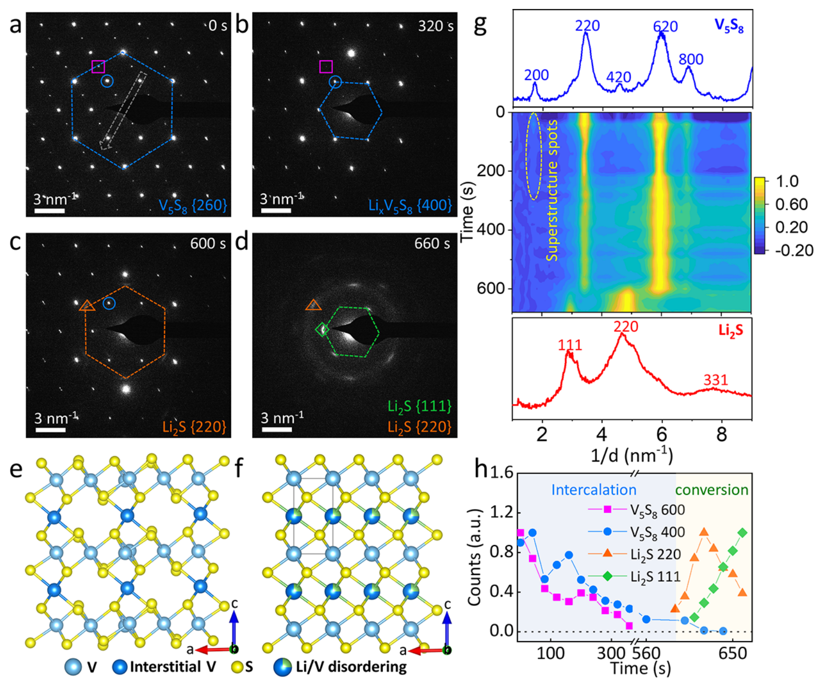

**Figure 2.** In situ SAED patterns tracking the structural evolution upon lithium insertion into the $V_5S_8$ nanosheet. (**a**−**d**) Time-lapsed SAED patterns along the [001] direction of lithiated $V_5S_8$. (e) Atomistic model of $V_5S_8$ and (f) $Li_3V_5S_8$. The gray, purple, yellow, and mixture balls indicate the V, interstitial V, S, and Li/V random arrangement. (g) Radial intensity profiles of the diffraction reflections derived from Movie S2. The top and the bottom planes show the diffraction peaks of $V_5S_8$ and $Li_2S$, respectively. (h) Extracted diffraction intensities of $V_5S_8$, $Li_xV_5S_8$, and $Li_2S$ are plotted as a function of time. The blue circles, pink squares, orange triangles, and green diamonds correspond to these label shapes in (a−d).

to 8.0 A $g^{-1}$, the specific charge capacity can maintain at 432 mAh $g^{-1}$ and recovers to 821 mAh $g^{-1}$ when the rate returns to 0.1 mAh $g^{-1}$. Ou et al. studied the electrochemical reaction mechanism of $V_5S_8$ and its reversibility during the electrochemical cycling by in/ex situ X-ray diffraction (XRD).[28] During the discharge, they observed an intercalation reaction to form $Li_xV_5S_8$ from open-circuit voltage to 0.45 V, followed by a conversion reaction to form $Li_2S$ and V from 0.45 to 0.01 V. At the charge process, $Li_xV_5S_8$ is formed from 0.01 to 1.7 V and the structure is restored to $V_5S_8$ from 1.7 to 3.0 V. However, how the ions react with the host atoms and migrate within $V_5S_8$ and how the reaction interface evolves, which are related to the electrochemical performance, have been rarely explored, thus motivating our study.

In this work, using in situ electron diffraction (ED) and high-resolution transmission electron microscopy (HRTEM) techniques, we have tracked the dynamical structural evolutions during the (de)lithiation of $V_5S_8$ from nanometer to an atomic scale. We find that the initial insertion of lithium ions is via an intercalation reaction, which triggers an order to antisite disorder transformation by destroying the orderings of the interstitial V. Such transition is found to be reversible, i.e., the extraction of lithium ions from $Li_xV_5S_8$ results in the recovery of the orderings of interstitial V atoms. The following

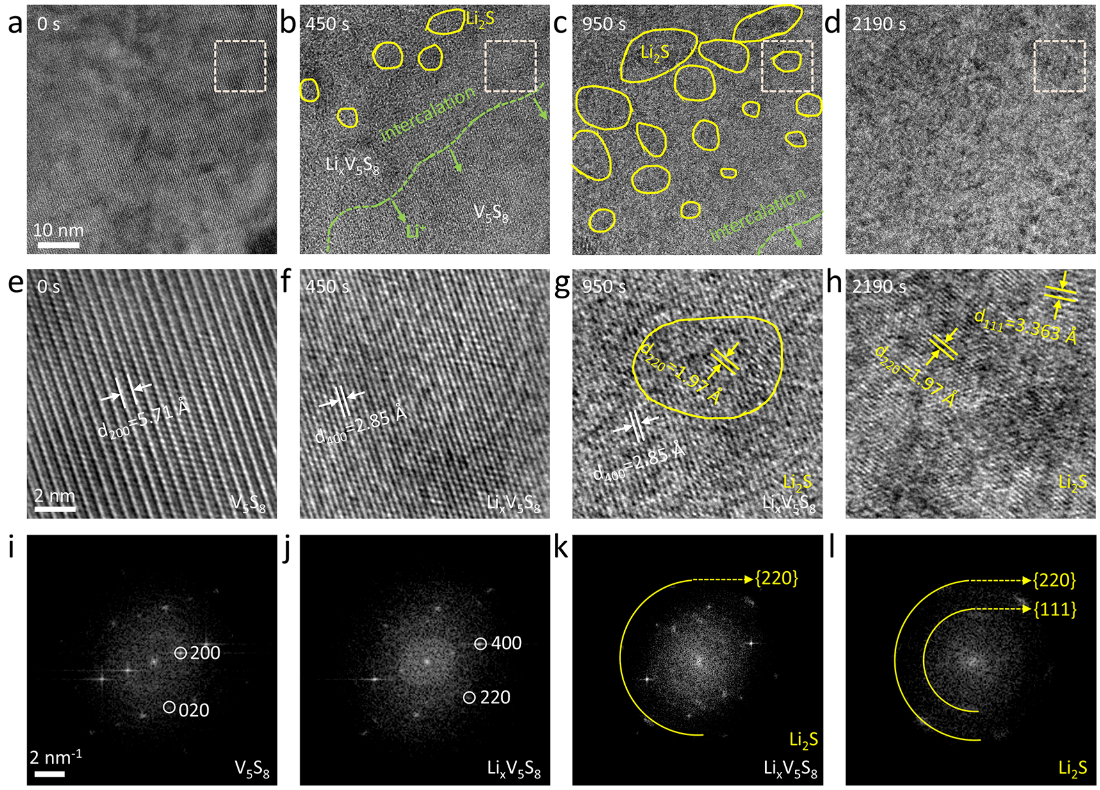


**Figure 3.** In situ HRTEM tracking the structural evolution during lithiation of $V_5S_8$. (a−d) Consecutive HRTEM images during the insertion of lithium into $V_5S_8$. The green dashed lines indicate the intercalation interface between $V_5S_8$ and $Li_xV_5S_8$. The yellow circles in (b) and (c) mark the nucleation of $Li_2S$. (e−h) Corresponding enlarged region highlighted by the white dashed squares in a−d, and (i−l) the corresponding FFT patterns.

conversion reaction involves the heterogeneous nucleation and topotactic growth of $Li_2S$ nanodomains. These findings reveal detailed structural evolutions during lithium migration in $V_5S_8$, indicating delicate and complex interactions between foreign ions and host atoms rather than a simple van der Waals interaction that may exist in TMD electrode materials.

## 2. RESULTS AND DISCUSSION

Figure 1a shows a typical schematic diagram of a nanosized solid battery to achieve (de)lithiation, including a Li counter electrode, a solid-state electrolyte (a passivation $Li_xO$ layer), and a $V_5S_8$ nanosheet as the working electrode. The $V_5S_8$ nanosheet is thinned from the bulk (Figure S1), which is synthesized by a chemical vapor transport method, as we have previously reported.[30] $V_5S_8$ is composed of distorted $VS_2$ layers intercalated with ordered V atoms, which occupy one-quarter of the octahedra sites (Figure 1a). Such interstitial V atoms cause superstructure diffraction spots (Figure 1b), compared with that of $VS_2$ (Figure S2). The acquired high-angle annular dark-field-scanning TEM (HAADF-STEM) image in Figure 1c is consistent with the atomistic structure along the [001] rather than the [100] zone axis despite their ED patterns being quite similar (Figure S3). The bright and dark atom columns are identified as V and S, respectively. Upon lithium insertion, a clear phase boundary between $Li_xV_5S_8$ and $V_5S_8$ can be observed, as shown in Figure 1d and Movie S1. As the lithiation progresses, the reaction gradually propagates from the surface to internal. We further acquire the diffusivity of the lithium ion (Figure 1e), according to the equation $D = d^2/2t$,[31] where $D$ is the diffusivity, $t$ is the diffusion time, and $d$ is the diffusion distance. The measured diffusivity is based on the migration of the reaction front, indicating the lithium diffusion in $V_5S_8$. The calculated diffusivity is about $10^{-13}$–$8 \times 10^{-13}$ $cm^2\ s^{-1}$, which is comparable to the electrochemically measured diffusivity ($6.168 \times 10^{-13}$–$8.285 \times 10^{-13}$ $cm^2\ s^{-1}$).[28] The valley at 100 s is likely caused by the change of a worse contact between $Li_2O$ and $V_5S_8$. More accurate Li diffusion coefficients in different phases can be obtained by the galvanostatic intermittent titration technique.

To investigate the structural evolutions during lithium ions intercalation, we carried out time-series in situ electron diffraction experiments, as shown in Figure 2a−d and Movie S2. The SAED pattern (Figure 2a) indicates a good single crystalline structure of $V_5S_8$. Upon the insertion of lithium ions, we observe that the superstructure diffraction spots gradually disappear (Figure 2b). The superstructure reflections are caused by ordered interstitial V atoms; thus, its disappearance suggests that such periodic interstitial V arrangement is damaged and all octahedral sites within the interlayer are randomly occupied by lithium or V,[32] as illustrated in Figure 2e−f. The crystal symmetry of $V_5S_8$ is monoclinic (space group: $F2/1m$), while $Li_xV_5S_8$ with disordered V is hexagonal (space group: $P\bar{3}m1$).[33] The simulated ED pattern of such a Li/V random structure can match with experimental one (Figure S4). In contrast, the superstructure can be maintained for 2 h under the pure electrical field (Figure S5 and Movie S3), further suggesting that the disappearance of the superstructure is not caused by the electrical field and the electron beam irradiation at low doses but related to lithium insertion. With more lithium ions insertion, we observe the formation of $Li_2S$ (JCPDS No. 23-



https://dx.doi.org/10.1021/acsami.0c08428
ACS Appl. Mater. Interfaces 2020, 12, 36320−36328

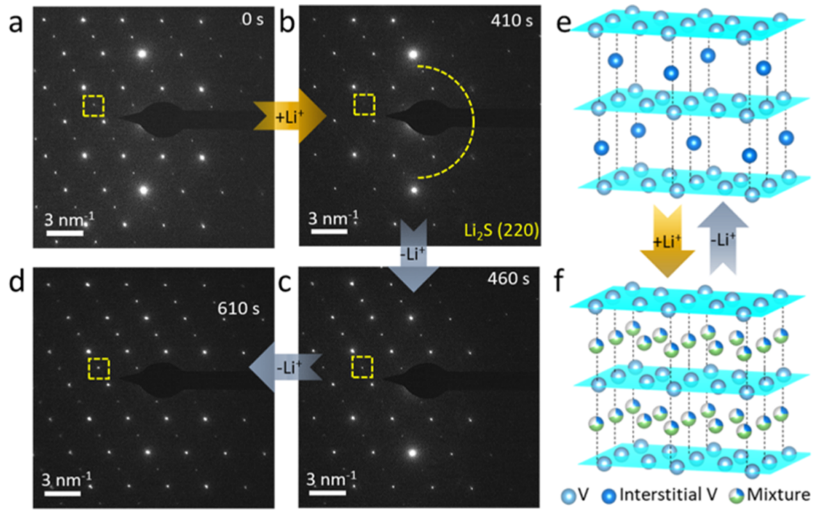


**Figure 4.** Reversible V ordering and disordering during lithium-ion migration in $V_5S_8$. (a, b) Time-series SAED showing lithium interaction and (c, d) extraction process. Lithiation is achieved using a −2 V voltage until the appearance of $Li_2S$, indicated by the yellow arc at 410 s in (b). Then, the voltage is changed to be +4 V to extract lithium. The yellow squares highlight the gradual disappearance and reappearance of the characteristic superstructure reflection. (e, f) Atomistic models of $V_5S_8$ and $Li_xV_5S_8$. Sulfur atoms are omitted for a better visualization of V atoms.

0369), indicating the start of the conversion reaction (Figure 2c). The $Li_2S$ {220} crystal planes are formed prior to {111} planes (Figure 2c,d). Interestingly, the newly formed $Li_2S$ maintains crystallographic integrity with $V_5S_8$ (highlighted by the hexagons), indicating that the nucleation and growth of $Li_2S$ are coherent to the pristine $V_5S_8$ structure.

The whole lithiation reaction is further examined by acquiring the radial intensity profiles (Figure 2g) of the diffraction reflections derived from Movie S2. It is observed that the superstructure peak (200) gradually disappears within ∼320 s. Basically, the in-plane crystal parameter is almost unchanged in the intercalation process (Figure S6). The formed $Li_xV_5S_8$ shows an increased interlayer spacing (∼2.6%) compared with $V_5S_8$ based on the previous XRD results.[28] Finally, the peaks of $Li_xV_5S_8$ disappear and then the (220) and (111) peaks of $Li_2S$ appear sequentially. After a deep lithiation, metal V is formed (Figure S7). Based on the changes of in/out-plane crystal parameters, the volume expansion during the intercalation process is about 2.6%. The conversion reaction always shows more obvious volume expansion, as observed during the lithiation of $Co_3O_4$.[34] However, $V_5S_8$ we used for in situ TEM is a large micron sheet (Figure 1d), making it difficult to identify the morphology changes caused by the volume expansion. The diffraction intensities of $V_5S_8$, $Li_xV_5S_8$, and $Li_2S$ are extracted in Figure 2h, presenting the whole reaction process that is initiated from an intercalation reaction to form interstitial-V-disordered $Li_xV_5S_8$, followed by the conversion reaction to form $Li_2S$ and V. The corresponding reaction equations can be expressed as

$$\text{intercalation: } V_5S_8 + x\mathrm{Li}^+ + xe^- \rightarrow \mathrm{Li}_xV_5S_8$$

$$\text{conversion: } \mathrm{Li}_xV_5S_8 + (16 - x)\mathrm{Li}^+ + e^- \rightarrow 8\mathrm{Li}_2S + 5V$$

The overall reaction mechanism is similar to previous in situ XRD results[28] that are initiated with intercalation and followed by a conversion reaction. However, our in situ TEM experiments provide more microscopic structural insights that the inserted lithium ions can destroy the orderings of the interstitial V and the formed $Li_2S$ maintains the crystallographic integrity with $Li_xV_5S_8$.

To further reveal local structural evolutions, time-series HRTEM images are recorded in Figure 3a−h. Figure 3a is a typical HRTEM image of $V_5S_8$ viewing along the [001] direction. Due to the orderings of interstitial V atoms, the pristine $V_5S_8$ features superstructure stripes (Figure 3e) and diffraction spots (Figure 3i). Upon the lithium insertion, such superstructure stripes and diffraction reflections disappear and the corresponding plane distance (2.85 Å) (Figure 3b,f,j) becomes one-half of the pristine one (5.71 Å), indicating the loss of the orderings of interstitial V. We can observe the intercalation interface between $V_5S_8$ and $Li_xV_5S_8$ as well as the formation of $Li_2S$ nanodomains (Figure 3b). The priority to forming the $Li_2S$ {220} plane is again observed (Figure 3c,g,k). Interestingly, we find heterogeneous nucleation of $Li_2S$ during the conversion reaction marked by the yellow circles in Figure 3b,c. The size of $Li_2S$ nanodomains ranges from 3 to 9 nm near the reaction front and grows larger away from the reaction front (12−18 nm). From the enlarged view of a small $Li_2S$ domain (Figure 3g), we can observe that the clear lattice stripes of the $Li_2S$ (220) plane maintain a topotactic relationship with the $Li_xV_5S_8$ (400) plane. These small $Li_2S$ domains grow larger and larger, and finally, the structure totally transforms into $Li_2S$ (Figure 3h,l). Note that $Li_2S$ nanodomains are formed near the interface (Figure 3b,c) between the pristine $V_5S_8$ and $Li_xV_5S_8$, which suggests that bulk $V_5S_8$ is partially inserted and then conversed rather than fully intercalated and then converted. Such nonequilibrium lithiation has also been observed in $Fe_3O_4$[35] and $Co_3O_4$[34] nanoparticles, which is influenced by discharging rates. At a low rate, the conversion reaction starts after the full intercalation while the intercalation reaction can be overwhelmed by the conversion reaction at a high rate.[34] Accordingly, an effective controlling the degree of the lithiation can be achieved by regulating the discharging rate for these intercalation-conversion-type electrode materials.

For rechargeable LIBs, it is a prerequisite to reversibly insert lithium ions into host materials. We find that once the insertion of lithium ions into $V_5S_8$ is controlled within the intercalation range, the lithium ions in $Li_xV_5S_8$ can be partly extracted (Movie S4). We first insert lithium ions into $V_5S_8$ by


https://dx.doi.org/10.1021/acsami.0c08428
ACS Appl. Mater. Interfaces 2020, 12, 36320−36328

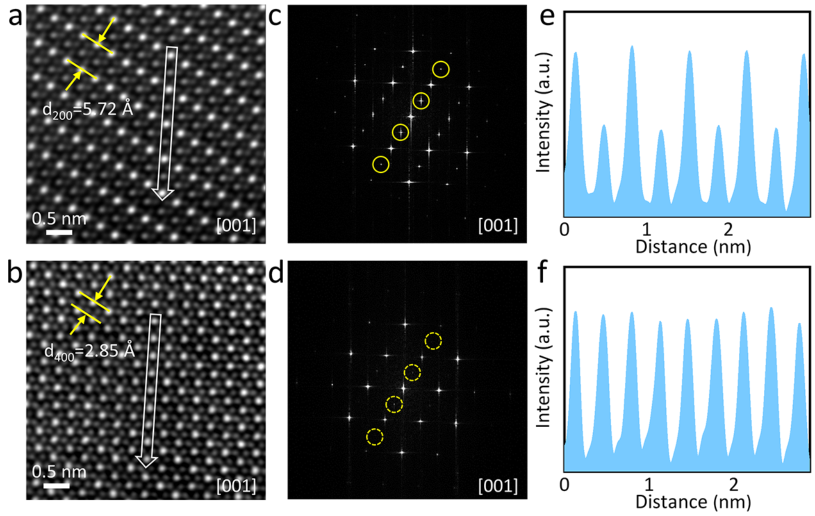


**Figure 5.** Atomic-scale observation of the superstructure-to-nonsuperstucture transition. (a, b) HAADF-STEM images of the pristine $V_5S_8$ and the structure after electron beam irradiation. The raw pristine images are shown in Figure S11. (c, d) Corresponding FFT patterns. The yellow circles highlight the superstructure diffraction spots. (e, f) Atom columns contrast extracted from the line profiles in (a) and (b), as shown by white arrows.

applying a −2 V voltage. Upon lithium insertion, the superstructure diffraction spots gradually disappear (Figure 4a,b). Though the zone axis has changed a little (Figure 4a,b), the zone axis titling effect on the disappearance of superstructure spots can be eliminated, as explained in Figure S8. Once the diffraction spots of $Li_2S$ appear (Figure 4b), indicating the conversion reaction starts, the applied voltage is changed to be + 4 V to extract the lithium ions in $Li_xV_5S_8$. It is found that the disappeared superstructure reflections gradually reappear (Figure 4c,d), suggesting that the random V becomes ordered due to the extraction of lithium ions. Such reversible intercalation reaction, as illustrated in Figure 4e,f, can promise good cycling performance when lithiation is controlled within the intercalation range, which has been used to improve the cycling performance of $VS_2$.[36]

It is known that the battery performance is largely determined by the structural evolutions during the reaction for LIBs. By in situ TEM, we investigate the reaction pathways and phase transformations of $V_5S_8$. During the lithiation of $V_5S_8$, we find the orderings of the interstitial V is destroyed since the inserted lithium can take up the position of interstitial V and pull V to the neighboring octahedral sites due to Coulomb repulsion,[37] enabling Li and V to occupy the octahedral sites randomly. Indeed, the interstitial V in $V_5S_8$ can migrate to the near octahedral sites above 800 °C, transforming into a $CdI_2$-type structure.[32] Then, the octahedral sites within S−V−S layers become equivalent and vacancies and cations become randomly distributed, leading to a symmetry change from $F2/m$ to $P\bar{3}m1$.[33] The previous work reported that the ordered Na/vacancy superstructure within the interlayers in $NaCoO_2$ lowers Na diffusion coefficient even up to two orders of magnitude.[38] Based on the first-principles calculations, we also compare the diffusion barriers of lithium diffusing in the bulk $VS_2$ (without ordered V within the interlayers) and $V_5S_8$ (existing ordered V within the interlayers). The lithium diffusion barriers are about 0.26 eV in $VS_2$ and 0.42 eV in $V_5S_8$, as shown in Figure S9. The lower diffusion barrier in $VS_2$ suggests a fast lithium-ion diffusion, which is consistent with the electrochemical measurements that the lithium-ion diffusion coefficient in $V_5S_8$ ($6{-}8 \times 10^{-13}$ $cm^2\ s^{-1}$)[28] is 2−3 magnitude lower than that for $VS_2$ ($10^{-10}$−$10^{-12}$ $cm^2\ s^{-1}$).[39] Accordingly, the ordered V might generate a higher diffusion barrier that blocks the diffusion of lithium, and such a V disordered structure is likely beneficial to the diffusion of lithium.

To further confirm such disordering behavior at an atomic scale, we have mimicked the superstructure-nonsuperstucture transition under the high-energy electron beam, which has been widely used to track the dynamics of the phase transition.[40,41] Figure 5a is an atomically resolved HAADF-STEM image of the pristine $V_5S_8$. After beam illumination (see the Experimental Section for details), the superstructure lattices disappear with the plane distance becoming half of the pristine value (Figure 5a,b), accompanying with the disappearance of the superstructure reflections (Figure 5c,d). It is found that the uneven contrast of each atom column (Figure 5e) becomes more uniform (Figure 5f) after beam irradiation. In fact, the uneven contrast is caused by the interstitial V, which brings in a brighter contrast, as verified in the corresponding simulated HAADF STEM image (Figure S10). Under electron beam illumination, similar to that under the heat,[32] the interstitial V can migrate to the near equal octahedral sites; thus, vacancies and V become distributed randomly within this layer, leading to a uniform STEM contrast (Figure 5f).

Furthermore, our in situ TEM study has revealed a topotactic growth of $Li_2S$ during the conversion reaction of $V_5S_8$. The topotactic transition means that the crystal orientation of the product phase is correlated with the crystal orientation of the parent phase.[42,43] The orientation of the substrate determines the crystal orientation of the product, thus influencing the nucleation and growth of a new phase considering that different orientations might have different nucleation energy and growth driving energy.[44] Different from most topotactic transformations observed in the intercalation process via shuttling lithium ions between the tunnels of the host,[45] we find a topotactic conversion transformation, which plays a vital role in understanding the structure evolutions and the related battery performance. It is reported the topotactic cation diffusion through an invariant lattice of fluoride anions


https://dx.doi.org/10.1021/acsami.0c08428
ACS Appl. Mater. Interfaces 2020, 12, 36320−36328

governs the reversibility of the conversion reactions.[42] However, most studies failed to observe such behavior due to material or technique restrictions. For example, the powder and the polycrystalline materials show random orientations,[18,46] preventing the identification of the specific orientation relationship. Also, in situ XRD techniques provide the information of a series of equivalent planes rather than one specific one. Thus, it is beneficial to clarify more information about such topotactic transformation by in situ TEM techniques of the single-crystal battery materials.

We also compare the reaction mechanism of $V_5S_8$ with other TMDs. Similar to $MoS_2$[11,13] and $TiS_2$,[16,17] the reaction process of $V_5S_8$ proceeds via a sequence of intercalation and conversion reactions. The difference lies in the behaviors of the superstructures. The lithiation of $MoS_2$ and $TiS_2$ enables the formation of superstructures due to the distortion of Mo[11] or the ordered lithium insertion.[16] $V_5S_8$ itself shows the feature of superstructures due to the ordered interstitial V. Because of the Li−V interactions, the inserted lithium ions can destroy such V orderings with the disappearance of the superstructure. Similarly, the insertion of sodium into $MoS_2$ enables the formation of superstructure due to the ordered Na occupation,[47] while the insertion of sodium into $V_5S_8$ is expected to destroy the superstructure because of Na−V interactions.

## 3. CONCLUSIONS

In summary, we have investigated the lithiation mechanism of $V_5S_8$ by in situ TEM at an atomic scale. It is found that the lithiation process is initiated with a cationic order-to-disorder intercalation and followed by a conversion reaction. The insertion of lithium can destroy the orderings of interstitial V atoms. The intercalation reaction is found to be reversible, and the lithium ions can be extracted from $Li_xV_5S_8$ accompanying by the recovery of the superstructure. During the following conversion, heterogeneous $Li_2S$ nanodomains are formed, maintaining the crystallographic integrity with the $Li_xV_5S_8$. The reversibility of the conversion reactions seems to be highly dependent on these $Li_2S$ nanodomains and its topotactic growth feature, which might guide future material research to develop and identify high-energy materials with a reversible conversion reaction. This mechanistic understanding of $V_5S_8$ provides some insights for the intercalation-conversion type materials, which will guide the future development of high energy density materials.

## 4. EXPERIMENTAL SECTION

**4.1. Synthesis of $V_5S_8$.** The bulk $V_5S_8$ was synthesized by the chemical vapor transport method. The precursors (vanadium and sulfur powders) and transport agent (iodine) were first put into a silica ampule under argon. The ampule was then evacuated, sealed, and heated in a two-zone tube furnace to a temperature gradient of 850−1000 °C for 2 weeks before acquiring the bulk crystals.

**4.2. In Situ TEM Experiments.** In situ TEM experimental setup includes a $V_8S_5$ working electrode, a lithium metal as the counter electrode, and a thin layer $Li_xO$ as the solid electrolyte. The formed $Li_xO$ can serve as a solid-state electrolyte that allows the transport of $Li^+$ and prevents the transport of the electron since $Li_2O$ is a good $Li^+$ conductor and an electronic insulator with the diffusivity of $Li^+$ being $10^{-10}$ cm$^2$ s$^{-1}$ and a large band gap of ∼8 eV.[48] $V_5S_8$ used in this work was prepared by the mechanical polishing and ion-beam milling process using argon ion milling (Leica EM RES102). The ion milling process was carried out at 5 kV until a hole appeared, and then a low voltage (0.8 kV) was used to reduce the irradiation-damaged layers. The metal lithium was scratched using an electrochemically etched sharp tungsten tip. The electrical TEM specimen holder (PicoFemto) was sealed in an argon-filled glovebox and then transferred into the TEM column. During the transfer process, the lithium probe was exposed to the air to form $Li_xO$ on the surface. Basically, the exposure time was controlled within 5 s to obtain a 700−1000 nm $Li_xO$ layer.[48] The tungsten tip is driven by a piezo-ceramic manipulator to contact with $V_5S_8$. The lithiation of $V_5S_8$ was achieved by applying a small negative bias (−2 V) between the grounded tungsten probe and $V_5S_8$, while a positive bias (4 V) was employed to extract the lithium ions.

**4.3. Characterizations and Analysis.** Powder XRD pattern was obtained on D8 Advance diffractometer using Cu K$\alpha$ radiation (40 kV and 100 mA), and the SEM image was acquired by FEI Quanta 200F. In situ ED and HRTEM techniques were carried out at a dose rate of 2 and 800 e Å$^{-2}$ s$^{-1}$, respectively, using Tecnai F20 at 200 kV equipped with a OneView IS (Gatan) camera. The atomically resolved STEM images were acquired using an aberration-corrected FEI Titan Themis G2 microscope operated at an accelerating voltage of 300 kV with a beam current of 50 pA, a convergence semiangle of 21 mrad, and a collection semiangle snap in the range of 80−380 mrad. The electron beam irradiation experiment was carried out using the STEM area scanning mode at 100 pA with an 18 nm × 18 nm scanning area. The corresponding dose rate is estimated to be 1.92 × $10^7$ e Å$^{-2}$ s$^{-1}$.[49] The movies were prepared from time-series images. FFT patterns and the line profiles were obtained using DigitalMicrograph (Gatan) software. The simulation of the ED patterns was performed using Crystalmaker software, and the atomistic models were obtained by Vesta software. The radial intensity profiles are prepared by ImageJ software. The STEM simulation was carried out by Kirkland with COMPUTEM software.[50] The plots were drawn using Origin 2016.

**4.4. First-principles Calculations.** The structures of the bulk $V_5S_8$, $VS_2$, and their Li-adsorbed compounds were fully optimized by Vienna Ab initio Simulation Package (VASP).[51] The climbing image nudged elastic band method was implemented in the VASP transition state tools to calculate the diffusion barriers of lithium ions.[52,53] In our calculation, density functional theory with a cutoff energy of 500 eV was used; the generalized gradient approximation combined with the Perdew−Burke−Ernzerh form and the plane-wave basis set with the projector-augmented wave pseudopotential were adopted; the *k*-point mesh was sampled by the Monkhorst−Pack method with a separation of 0.02 Å$^{-1}$; and the convergence thresholds were $10^{-6}$ eV for energy and $10^{-3}$ eV/Å for a force to get the precise results.[54,55]

## ■ ASSOCIATED CONTENT

### Supporting Information

The Supporting Information is available free of charge at https://pubs.acs.org/doi/10.1021/acsami.0c08428.

Structure and morphology of $V_5S_8$; comparison of $V_5S_8$ and $VS_2$; structure of $V_5S_8$; comparison of $V_5S_8$ and $Li_3V_5S_8$; structural evolutions under pure electrical field; plane distance changes during the lithiation of $V_5S_8$; formation of metal V; simulated ED patterns of $V_5S_8$; diffusion pathways and energy profiles; structure of $V_5S_8$ along the [001] direction; unfiltered HAADFSTEM images (PDF)

Migration of phase boundary between $Li_xV_5S_8$ and $V_5S_8$ (MP4)

Time-series in situ SAED patterns upon lithium ion insertion into $V_5S_8$ (MP4)

Superstructure maintained for 2 h at a dose rate of 2 e Å$^{-2}$ s$^{-1}$ under the pure electrical field (MP4)

Time-series SAED patterns showing lithium ion interaction and extraction process (MP4)



https://dx.doi.org/10.1021/acsami.0c08428
ACS Appl. Mater. Interfaces 2020, 12, 36320−36328

## AUTHOR INFORMATION


### Corresponding Authors

**Jing Lu** − *State Key Laboratory for Artificial Microstructure and Mesoscopic Physics, School of Physics, Peking University, Beijing 100871, China; Collaborative Innovation Center of Quantum Matter, Beijing 100871, China*; Email: jinglu@pku.edu.cn

**Liping Wang** − *School of Materials and Energy, University of Electronic Science and Technology of China, Chengdu 610054, China*; orcid.org/0000-0002-6412-266X; Email: lipingwang@uestc.edu.cn

**Junlei Qi** − *State Key Laboratory of Advanced Welding and Joining, Harbin Institute of Technology, Harbin 150001, China*; Email: jlqi@hit.edu.cn

**Peng Gao** − *Electron Microscopy Laboratory, School of Physics and International Center for Quantum Materials, School of Physics, Peking University, Beijing 100871, China; Collaborative Innovation Center of Quantum Matter, Beijing 100871, China*; orcid.org/0000-0003-0860-5525; Email: p-gao@pku.edu.cn

### Authors

**Shulin Chen** − *State Key Laboratory of Advanced Welding and Joining, Harbin Institute of Technology, Harbin 150001, China; Electron Microscopy Laboratory, School of Physics, Peking University, Beijing 100871, China*

**Chen Yang** − *State Key Laboratory for Artificial Microstructure and Mesoscopic Physics, School of Physics, Peking University, Beijing 100871, China*; orcid.org/0000-0001-9820-0833

**Ruiwen Shao** − *Beijing Advanced Innovation Center for Intelligent Robots and Systems, Institute of Convergence in Medicine and Engineering, Beijing Institute of Technology, Beijing 10081, China*

**Jingjing Niu** − *State Key Laboratory for Artificial Microstructure and Mesoscopic Physics, School of Physics, Peking University, Beijing 100871, China*

**Mei Wu** − *Electron Microscopy Laboratory, School of Physics and International Center for Quantum Materials, School of Physics, Peking University, Beijing 100871, China*

**Jian Cao** − *State Key Laboratory of Advanced Welding and Joining, Harbin Institute of Technology, Harbin 150001, China*

**Xiumei Ma** − *Electron Microscopy Laboratory, School of Physics, Peking University, Beijing 100871, China*

**Jicai Feng** − *State Key Laboratory of Advanced Welding and Joining, Harbin Institute of Technology, Harbin 150001, China*

**Xiaosong Wu** − *State Key Laboratory for Artificial Microstructure and Mesoscopic Physics, School of Physics, Peking University, Beijing 100871, China*; orcid.org/0000-0001-9224-9871

Complete contact information is available at: https://pubs.acs.org/10.1021/acsami.0c08428


### Author Contributions

S.C. and C.Y. contributed equally to this work. P.G., J.L., L.W., and J.L. conceived and supervised the project. S.C. performed in situ TEM experiments with the guidance of P.G. and help from R.S. and X.M.; C.Y. conducted the DFT calculations under the guidance of J.L.; J.N. grew the $V_5S_8$ crystals and performed SEM and XRD characterizations with the guidance from X.W.; M.W. prepared the TEM specimens. J.C., J.F., L.W., and J.Q. provided crystals. S.C., L.W., and P.G. wrote the manuscript, and all authors participated in the discussions.

### Notes

The authors declare no competing financial interest.

## ACKNOWLEDGMENTS

The work was supported by the Key-Area Research and Development Program of GuangDong Province (Grant No. 2018B010109009), National Natural Science Foundation of China (Grant Nos. 51672007, 11974023, 51575135, and U1537206), National Basic Research Program of China (Grant Nos. 2016YFA0300804 and 2016YFA0300903), Fundamental Research Funds for the Central Universities, China (Grant No. ZYGX2019Z008), Natural Science Foundation of Heilongjiang Province of China (Grant No. YQ2019E023), and "2011 Program" Peking-Tsinghua-IOP Collaborative Innovation Center of Quantum Matter. We acknowledge the Electron Microscopy Laboratory at Peking University for the use of electron microscopes and the high-performance computing platform of Peking University.

## REFERENCES


(1) Pomerantseva, E.; Bonaccorso, F.; Feng, X.; Cui, Y.; Gogotsi, Y. Energy Storage: The Future Enabled by Nanomaterials. *Science* **2019**, *366*, No. eaan8285.

(2) Choi, J. W.; Aurbach, D. Promise and Reality of Post-Lithium-Ion Batteries with High Energy Densities. *Nat. Rev. Mater.* **2016**, *1*, No. 16013.

(3) Guo, F.; Chen, P.; Kang, T.; Wang, Y.; Liu, C.; Shen, Y.; et al. Silicon-Loaded Lithium-Carbon Composite Microspheres as Lithium Secondary Battery Anodes. *Acta Phys.-Chim. Sin.* **2019**, *35*, 1365−1371.

(4) Cao, X.; Tan, C.; Zhang, X.; Zhao, W.; Zhang, H. Solution-Processed Two-Dimensional Metal Dichalcogenide-Based Nanomaterials for Energy Storage and Conversion. *Adv. Mater.* **2016**, *28*, 6167−6196.

(5) Tu, F.; Han, Y.; Du, Y.; Ge, X.; Weng, W.; Zhou, X.; Bao, J. Hierarchical Nanospheres Constructed by Ultrathin $MoS_2$ Nanosheets Braced on Nitrogen-Doped Carbon Polyhedra for Efficient Lithium and Sodium Storage. *ACS Appl. Mater. Interfaces* **2018**, *11*, 2112−2119.

(6) Chhowalla, M.; Shin, H. S.; Eda, G.; Li, L.; Loh, K. P.; Zhang, H. The Chemistry of Two-Dimensional Layered Transition Metal Dichalcogenide Nanosheets. *Nat. Chem.* **2013**, *5*, 263−275.

(7) Chen, J.; Chua, D. H. C.; Lee, P. S. The Advances of Metal Sulfides and in situ Characterization Methods beyond Li Ion Batteries: Sodium, Potassium, and Aluminum Ion Batteries. *Small Methods* **2020**, *4*, No. 1900648.

(8) Liu, Y.; He, X.; Hanlon, D.; Harvey, A.; Coleman, J. N.; Li, Y. Liquid Phase Exfoliated $MoS_2$ Nanosheets Percolated with Carbon Nanotubes for High Volumetric/Areal Capacity Sodium-Ion Batteries. *ACS Nano* **2016**, *10*, 8821−8828.

(9) Kim, S.; Yao, Z.; Lim, J.; Hersam, M. C.; Wolverton, C.; Dravid, V. P.; He, K. Atomic-Scale Observation of Electrochemically Reversible Phase Transformations in $SnSe_2$ Single Crystals. *Adv. Mater.* **2018**, *30*, No. 1804925.

(10) Ge, X.; Liu, S.; Qiao, M.; Du, Y.; Li, Y.; Bao, J.; Zhou, X. Enabling Superior Electrochemical Properties for Highly Efficient Potassium Storage by Impregnating Ultrafine Sb Nanocrystals within Nanochannel-Containing Carbon Nanofibers. *Angew. Chem., Int. Ed.* **2019**, *58*, 14578−14583.

(11) Wang, L.; Xu, Z.; Wang, W.; Bai, X. Atomic Mechanism of Dynamic Electrochemical Lithiation Processes of $MoS_2$ Nanosheets. *J. Am. Chem. Soc.* **2014**, *136*, 6693−6697.

(12) Wang, X.; Shen, X.; Wang, Z.; Yu, R.; Chen, L. Atomic-Scale Clarification of Structural Transition of $MoS_2$ upon Sodium Intercalation. *ACS Nano* **2014**, *8*, 11394−11400.

(13) Chen, S.; Wang, L.; Shao, R.; Zou, J.; Cai, R.; Lin, J.; Zhu, C.; Zhang, J.; Xu, F.; Cao, J.; Feng, J.; Qi, J.; Gao, P. Atomic Structure

and Migration Dynamics of $MoS_2/Li_XMoS_2$ Interface. *Nano Energy* **2018**, *48*, 560−568.
(14) Hwang, S.; Yao, Z.; Zhang, L.; Fu, M.; He, K.; Mai, L.; Wolverton, C.; Su, D. Multistep Lithiation of Tin Sulfide: An Investigation Using in Situ Electron Microscopy. *ACS Nano* **2018**, *12*, 3638−3645.
(15) Gao, P.; Wang, L.; Zhang, Y.; Huang, Y.; Liao, L.; Sutter, P.; Liu, K.; Yu, D.; Wang, E. High-Resolution Tracking Asymmetric Lithium Insertion and Extraction and Local Structure Ordering in $SnS_2$. *Nano Lett.* **2016**, *16*, 5582−5588.
(16) Han, B.; Chen, S.; Zou, J.; Shao, R.; Dou, Z.; Yang, C.; Ma, X.; Lu, J.; Liu, K.; Yu, D.; Wang, L.; Wang, H.; Gao, P. Tracking Sodium Migration in $TiS_2$ Using in Situ TEM. *Nanoscale* **2019**, *11*, 7474−7480.
(17) Fu, M.; Yao, Z.; Ma, X.; Dong, H.; Sun, K.; Hwang, S.; Hu, E.; Gan, H.; Yao, Y.; Stach, E. A.; Wolverton, C.; Su, D. Expanded Lithiation of Titanium Disulfide: Reaction Kinetics of Multi-Step Conversion Reaction. *Nano Energy* **2019**, *63*, No. 103882.
(18) Wang, X.; Yao, Z.; Hwang, S.; Pan, Y.; Dong, H.; Fu, M.; Li, N.; Sun, K.; Gan, H.; Yao, Y.; Aspuru-Guzik, A.; Xu, Q.; Su, D. In Situ Electron Microscopy Investigation of Sodiation of Titanium Disulfide Nanoflakes. *ACS Nano* **2019**, *13*, 9421−9430.
(19) He, K.; Yao, Z.; Hwang, S.; Li, N.; Sun, K.; Gan, H.; Du, Y.; Zhang, H.; Wolverton, C.; Su, D. Kinetically-Driven Phase Transformation During Lithiation in Copper Sulfide Nanoflakes. *Nano Lett.* **2017**, *17*, 5726−5733.
(20) Li, Q.; Xu, Y.; Yao, Z.; Kang, J.; Liu, X.; Wolverton, C.; Hersam, M. C.; Wu, J.; Dravid, V. P. Revealing the Effects of Electrode Crystallographic Orientation on Battery Electrochemistry via he Anisotropic Lithiation and Sodiation of $ReS_2$. *ACS Nano* **2018**, *12*, 7875−7882.
(21) Liu, D.; Shadike, Z.; Lin, R.; Qian, K.; Li, H.; Li, K.; Wang, S.; Yu, Q.; Liu, M.; Ganapathy, S.; Qin, X.; Yang, Q. H.; Wagemaker, M.; Kang, F.; Yang, X. Q.; Li, B. Review of Recent Development of in Situ/Operando Characterization Techniques for Lithium Battery Research. *Adv. Mater.* **2019**, *31*, No. 1806620.
(22) Gao, P. Nanosized Cu-Li Glass. *Sci. Bull.* **2018**, *63*, 1173.
(23) Jing, Y.; Zhou, Z.; Cabrera, C. R.; Chen, Z. Metallic $VS_2$ Monolayer: A Promising 2D Anode Material for Lithium Ion Batteries. *J. Phys. Chem. C* **2013**, *117*, 25409−25413.
(24) Zhou, J.; Wang, L.; Yang, M.; Wu, J.; Chen, F.; Huang, W.; Han, N.; Ye, H.; Zhao, F.; Li, Y.; Li, Y. Hierarchical $VS_2$ Nanosheet Assemblies: A Universal Host Material for the Reversible Storage of Alkali Metal Ions. *Adv. Mater.* **2017**, *29*, No. 1702061.
(25) Sun, R.; Wei, Q.; Sheng, J.; Shi, C.; An, Q.; Liu, S.; Mai, L. Novel Layer-By-Layer Stacked $VS_2$ Nanosheets with Intercalation Pseudocapacitance for High-Rate Sodium Ion Charge Storage. *Nano Energy* **2017**, *35*, 396−404.
(26) Xie, X.; Makaryan, T.; Zhao, M.; Van Aken, K. L.; Gogotsi, Y.; Wang, G. $MoS_2$ Nanosheets Vertically Aligned on Carbon Paper: A Freestanding Electrode for Highly Reversible Sodium-Ion Batteries. *Adv. Energy Mater.* **2016**, *6*, No. 1502161.
(27) Yang, C.; Ou, X.; Xiong, X.; Zheng, F.; Hu, R.; Chen, Y.; Liu, M.; Huang, K. $V_5S_8$-Graphite Hybrid Nanosheets as a High Rate-Capacity and Stable Anode Material for Sodium-Ion Batteries. *Energy Environ. Sci.* **2017**, *10*, 107−113.
(28) Ou, X.; Liang, X.; Zheng, F.; Pan, Q.; Zhou, J.; Xiong, X.; Yang, C.; Hu, R.; Liu, M. Exfoliated $V_5S_8$/graphite Nanosheet with Excellent Electrochemical Performance for Enhanced Lithium Storage. *Chem. Eng. J.* **2017**, *320*, 485−493.
(29) Li, L.; Zhang, W.; Wang, X.; Zhang, S.; Liu, Y.; Li, M.; Zhu, G.; Zheng, Y.; Zhang, Q.; Zhou, T.; Pang, W. K.; Luo, W.; Guo, Z.; Yang, J. Hollow-Carbon-Templated Few-Layered V5S8 Nanosheets Enabling Ultrafast Potassium Storage and Long-Term Cycling. *ACS Nano* **2019**, *13*, 7939−7948.
(30) Niu, J.; Li, Z.; Yang, W.; Yan, D.; Chen, S.; Zhang, Z.; Zhang, Y.; Ren, X.; Gao, P.; Shi, Y.; Yu, D.; Wu, X. V5S8: A Kondo Lattice Based on Intercalation of Van Der Waals Layered Transition Metal Dichalcogenide. arXiv:1809.04213. arXiv.org e-Print archive. https://arxiv.org/abs/1809.04213.
(31) Wang, L.; Wu, Z.; Zou, J.; Gao, P.; Niu, X.; Li, H.; Chen, L. Li-Free Cathode Materials for High Energy Density Lithium Batteries. *Joule* **2019**, *3*, 2086−2102.
(32) Nakazawa, H.; Saeki, M.; Nakahira, M. Order-Disorder Phenomena of Cationic Vacancies in a Vanadium Sulphide, $V_5S_8$. *J. Less Common Met.* **1975**, *40*, 57−63.
(33) Shao, R.; Chen, S.; Dou, Z.; Zhang, J.; Ma, X.; Zhu, R.; Xu, J.; Gao, P.; Yu, D. Atomic-Scale Probing of Reversible Li Migration in $1T\text{-}V_{1+X}Se_2$ and the Interactions Between Interstitial V and Li. *Nano Lett.* **2018**, *18*, 6094−6099.
(34) Li, J.; He, K.; Meng, Q.; Li, X.; Zhu, Y.; Hwang, S.; Sun, K.; Gan, H.; Zhu, Y.; Mo, Y.; Stach, E. A.; Su, D. Kinetic Phase Evolution of Spinel Cobalt Oxide During Lithiation. *ACS Nano* **2016**, *10*, 9577−9585.
(35) He, K.; Zhang, S.; Li, J.; Yu, X.; Meng, Q.; Zhu, Y.; Hu, E.; Sun, K.; Yun, H.; Yang, X.; Zhu, Y.; Gan, H.; Mo, Y.; Stach, E. A.; Murray, C. B.; Su, D. Visualizing Non-Equilibrium Lithiation of Spinel Oxide Via in Situ Transmission Electron Microscopy. *Nat. Commun.* **2016**, *7*, No. 11441.
(36) Cai, L.; Zhang, Q.; Mwizerwa, J. P.; Wan, H.; Yang, X.; Xu, X.; Yao, X. Highly Crystalline Layered $VS_2$ Nanosheets for All-Solid-State Lithium Batteries with Enhanced Electrochemical Performances. *ACS Appl. Mater. Interfaces* **2018**, *10*, 10053−10063.
(37) Yin, S.; Grondey, H.; Strobel, P.; Huang, H.; Nazar, L. F. Charge Ordering in Lithium Vanadium Phosphates: Electrode Materials for Lithium-Ion Batteries. *J. Am. Chem. Soc.* **2003**, *125*, 326−327.
(38) Shu, G. J.; Chou, F. C. Sodium-Ion Diffusion and Ordering in Single-Crystal P2-$NaCoO_2$. *Phys. Rev. B* **2008**, *78*, No. 52101.
(39) Meng, Y.; Zhao, Y.; Wang, D.; Yang, D.; Gao, Y.; Lian, R.; Chen, G.; Wei, Y. Fast $Li^+$ Diffusion in Interlayer-Expanded Vanadium Disulfide Nanosheets for $Li^+/Mg^{2+}$ Hybrid-Ion Batteries. *J. Mater. Chem. A* **2018**, *6*, 5782−5788.
(40) Gao, P.; Ishikawa, R.; Tochigi, E.; Kumamoto, A.; Shibata, N.; Ikuhara, Y. Atomic-Scale Tracking of a Phase Transition from Spinel to Rocksalt in Lithium Manganese Oxide. *Chem. Mater.* **2017**, *29*, 1006−1013.
(41) Zhu, L.; Jin, X.; Zhang, Y.; Du, S.; Liu, L.; Rajh, T.; Xu, Z.; Wang, W.; Bai, X.; Wen, J.; Wang, L. Visualizing Anisotropic Oxygen Diffusion in Ceria Under Activated Conditions. *Phys. Rev. Lett.* **2020**, *124*, No. 56002.
(42) Xiao, A. W.; Lee, H. J.; Capone, I.; Robertson, A.; Wi, T.; Fawdon, J.; Wheeler, S.; Lee, H.; Grobert, N.; Pasta, M. Understanding the Conversion Mechanism and Performance of Monodisperse $FeF_2$ Nanocrystal Cathodes. *Nat. Mater.* **2020**, *19*, 644−654.
(43) Shannon, R. D.; Rossi, R. C. Definition of Topotaxy. *Nature* **1964**, *202*, 1000−1001.
(44) Tian, N.; Zhou, Z.; Sun, S.; Ding, Y.; Wang, Z. L. Synthesis of Tetrahexahedral Platinum Nanocrystals with High-Index Facets and High Electro-Oxidation Activity. *Science* **2007**, *316*, 732−735.
(45) Whittingham, M. S. Ultimate Limits to Intercalation Reactions for Lithium Batteries. *Chem. Rev.* **2014**, *114*, 11414−11443.
(46) Hwang, S.; Yao, Z.; Zhang, L.; Fu, M.; He, K.; Mai, L.; Wolverton, C.; Su, D. Multistep Lithiation of Tin Sulfide: An Investigation Using in Situ Electron Microscopy. *ACS Nano* **2018**, *12*, 3638−3645.
(47) Li, Q.; Yao, Z.; Wu, J.; Mitra, S.; Hao, S.; Sahu, T. S.; Li, Y.; Wolverton, C.; Dravid, V. P. Intermediate Phases in Sodium Intercalation into $MoS_2$ Nanosheets and their Implications for Sodium-Ion Batteries. *Nano Energy* **2017**, *38*, 342−349.
(48) Liu, X. H.; Huang, J. Y. In Situ TEM Electrochemistry of Anode Materials in Lithium Ion Batteries. *Energy Environ. Sci.* **2011**, *4*, 3844−3860.
(49) Johnston-Peck, A. C.; DuChene, J. S.; Roberts, A. D.; Wei, W. D.; Herzing, A. A. Dose-Rate-Dependent Damage of Cerium Dioxide in the Scanning Transmission Electron Microscope. *Ultramicroscopy* **2016**, *170*, 1−9.

(50) Kirkland, E. J. *Advanced Computing in Electron Microscopy*; Plenum Press: New York, 1998.
(51) Kresse, G.; Hafner, J. Ab Initio Molecular Dynamics for Liquid Metals. *Phys. Rev. B* **1993**, *47*, 558.
(52) Henkelman, G.; Uberuaga, B. P.; Jónsson, H. A Climbing Image Nudged Elastic Band Method for Finding Saddle Points and Minimum Energy Paths. *J. Chem. Phys.* **2000**, *113*, 9901−9904.
(53) Henkelman, G.; Jónsson, H. Improved Tangent Estimate in the Nudged Elastic Band Method for Finding Minimum Energy Paths and Saddle Points. *J. Chem. Phys.* **2000**, *113*, 9978−9985.
(54) Zhang, X.; Yang, C.; Pan, Y.; Weng, M.; Xu, L.; Liu, S.; Yang, J.; Yan, J.; Li, J.; Shi, B.; et al. Monolayer GaS with High Ion Mobility and Capacity as a Promising Anode Battery Material. *J. Mater. Chem. A* **2019**, *7*, 14042−14050.
(55) Yang, C.; Zhang, X.; Ma, J.; Shi, B.; Zhang, H.; Xu, L.; Yang, J.; Liu, S.; Quhe, R.; Pan, F.; et al. Ultrahigh Capacity of Monolayer Dumbbell $C_4N$ as a Promising Anode Material for Lithium-Ion Battery. *J. Electro. Chem. Soc.* **2020**, *167*, No. 020538.


https://dx.doi.org/10.1021/acsami.0c08428
*ACS Appl. Mater. Interfaces* 2020, 12, 36320−36328